Oceanic three-dimensional Lagrangian coherent structures: A study of a mesoscale eddy in the Benguela upwelling region

João H. Bettencourt [*], Cristóbal López, Emilio Hernández-García

IFISC (CSIC-UIB), Instituto de Física Interdisciplinar y Sistemas Complejos, Campus Universitat de les Illes Balears, E-07122 Palma de Mallorca, Spain

ARTICLE INFO

ABSTRACT

We study three dimensional (3D) oceanic Lagrangian coherent structures (LCSs) in the Benguela upwelling region obtained from an output of the regional ocean modeling system (ROMS). To do that, we first computed finite-size Lyapunov exponent (FSLE) fields in the region volume that characterize mesoscale stirring and mixing. Average FSLE values generally decreased with depth, but there was a local maximum at a depth of approximately 100 m. LCSs are extracted as the ridges of the calculated FSLE fields. They present a "curtain-like" geometry in which the strongest attracting and repelling structures appear as quasivertical surfaces. LCSs around a particular cyclonic eddy, pinched off from the upwelling front, are also calculated. The LCSs are confirmed to provide pathways and barriers to transport into and out of the eddy.

© 2012 Elsevier Ltd. All rights reserved.

1. Introduction

Mixing and transport processes are fundamental to the physical, chemical and biological properties of oceans. From plankton dynamics to the development of pollutant spills, there is a wide range of practical issues that benefit from understanding and modeling these processes. Although mixing and transport occur at a wide range of scales in the oceans, mesoscale and sub-mesoscale variability are known to play very important roles (Thomas et al., 2008; Klein and Lapeyre, 2009).

Mesoscale eddies are especially important in this respect because of their long life in oceanic flows and their stirring and mixing properties. In the southern Benguela region, for instance, cyclonic eddies shed from the Agulhas current can transport and exchange warm waters between the Indian Ocean and the South Atlantic (Byrne et al., 1995; Lehahn et al., 2011). Moreover, mesoscale eddies have been shown to drive important biogeochemical processes in the ocean such as the vertical flux of nutrients into the euphotic zone (McGillicuddy et al., 1998; Oschlies and Garçon, 1998). Another effect of eddy activity appears to be the intensification of mesoscale and sub-mesoscale variability due to the filamentation process, where strong tracer gradients are created by the stretching of tracers in the shear- and strain-dominated regions in between eddy cores (Elhmaïdi et al., 1993). Studies of the vertical structure of such eddies in the Benguela region (e.g., Doglioli

et al., 2007; Rubio et al., 2009) have shown that the eddies can extend up to 1000 m deep.

In recent decades, new developments in the description and modeling of oceanic mixing and transport from a Lagrangian viewpoint have emerged (Mariano et al., 2002; Lacasce, 2008). These Lagrangian approaches have become more and more frequently used due to the increased availability of detailed knowledge of the velocity field from Lagrangian drifters, satellite measurements and computer models. In particular, the very relevant concept of the Lagrangian coherent structure (LCS) (Haller, 2000; Haller and Yuan, 2000) is becoming crucial for the analysis of transport in ocean flows. LCSs are structures that separate the flow into regions with different dynamical behavior. They provide a general geometric view of flow dynamics, acting as a (time-dependent) roadmap for the flow. They are templates serving as proxies to, for instance, barriers and avenues to transport or eddy boundaries (Boffetta et al., 2001; Haller and Yuan, 2000; Haller, 2002; d'Ovidio et al., 2004; d'Ovidio et al., 2009; Mancho et al., 2006).

The relevance of the 3D structure of LCSs has begun to be explored in atmospheric contexts (duToit and Marsden, 2010; Tang et al., 2011; Tallapragada et al., 2011). In the context of oceanic flows, however, the identification of LCSs and the study of their role in the transport of biogeochemical tracers has primarily been restricted to the oceans surface (d'Ovidio et al., 2004; Waugh et al., 2006; d'Ovidio et al., 2009; Beron-Vera et al., 2008). This is mainly due to two reasons: (a) vertical tracer displacement is usually very small compared to horizontal displacement; and (b) satellite data of any quantity (temperature, chlorophyll, altimetry for velocity, etc.) are only available for the ocean surface.

* Corresponding author. Tel.: +34 971259905.
E-mail address: joaob@ifisc.uib-csic.es (J.H. Bettencourt).

Oceanic flows can be considered 2D because there is a great disparity between the horizontal and vertical length scales and flows are strongly stratified due to the Earth's rotation. There are, however, areas in the ocean where vertical motion is fundamental. One area is the so-called upwelling regions, which are the most biologically active marine zones in the world (Rossi et al., 2008; Pauly and Christensen, 1995). The reason for this activity is the Ekmann pumping mechanism. Close to the coast, there is a surface upwelling of deep, cold waters that are rich in nutrients, inducing a high concentration of plankton. Typically, the vertical velocities in upwelling regions are much greater than in the open ocean, but still one order of magnitude smaller than the horizontal velocities in the same area. Another example of locations where there are significant vertical processes is mesoscale eddies boundaries that produce submesoscale structures (frontogenesis), which are responsible for strong ageostrophic vertical processes in addition to the vertical exchange that is thought to occur in the eddy interior (Klein and Lapeyre, 2009). Thus, the identification of the 3D LCSs in these areas, as well as understanding their correlations with biological activity, is crucial. Another reason to include the third dimension in LCS studies is to investigate the vertical variation in LCS properties.

The primary objective of this paper is the characterization of 3D LCSs extracted from an upwelling region, the Benguela area in the southern Atlantic Ocean. To achieve this goal, we use finite-size Lyapunov exponents (FSLEs). FSLEs (Aurell et al., 1997; Artale et al., 1997) measure the separation rate of fluid particles between two given distance thresholds. LCSs are computed as the ridges of the FSLE field (d'Ovidio et al., 2004; Molcard et al., 2006; Haza et al., 2008; d'Ovidio et al., 2009; Poje et al., 2010; Haza et al., 2010). The rigorous definition of an LCS as a ridge of a Lagrangian stretching measure was given for the finite-time Lyapunov exponents (FTLEs), which are closely related to FSLEs, in Shadden et al. (2005) and Lekien et al. (2007). More recently, hyperbolic LCSs have been defined independently of such stretching measures by Haller (2011). Following many previous studies (d'Ovidio et al., 2004; Molcard et al., 2006; d'Ovidio et al., 2009; Branicki and Wiggins, 2009), we adapt the mathematical results for finite-time Lyapunov exponents (FTLEs) to FSLEs, assuming them to be valid. In particular, we assume that LCSs are identified with ridges (Haller, 2001), i.e., the local extrema of the FTLE field. We also expect, in accordance with the results in Shadden et al. (2005) and Lekien et al. (2007) for FTLEs, that the material flux through these LCSs is small and that LCSs are transported by the flow as quasi-material surfaces.

To confirm our identification of LCSs as the ridges of the FSLE field, we perform (in Section 3) direct particle trajectory integrations that show that the computed LCSs indeed organize the tracer flow. In our work, we will emphasize the numerical methodology because up to now, FSLEs have only been computed for the marine surface (an exception is Özgökmen et al. (2011)). We then focus on a particular eddy that is very prominent in the area within the chosen temporal window and study the stirring and mixing occurring in its vicinity. Some previous results for Lagrangian eddies were obtained by Branicki and Kirwan (2010) and Branicki et al. (2011), applying the methodology of lobe dynamics and the turnstile mechanism to eddies pinched off from the Loop Current. In this paper, we focus on FSLE fields and the associated particle trajectories to study transport into and out of the chosen mesoscale eddy. Because this is a first attempt to study 3D oceanic LCSs, more general results (for Benguela and other upwelling regions) are left for future work.

To circumvent the lack of appropriate observational data in the vertical direction, we use velocity fields from a numerical simulation. They are high resolution simulations from the ROMS model (see Section 2 below) and are thus appropriate for studying regional-medium scale basins.

The paper is organized as follows: in Section 2, we describe the data and methods. In Section 3, we present our results. Section 4 contains a discussion of the results, and Section 5 summarizes our conclusions.

2. Data and methods

2.1. Velocity data set

The Benguela ocean region is situated off of the west coast of southern Africa. It is characterized by a vigorous coastal upwelling regime forced by equatorward winds, substantial mesoscale activity of the upwelling front in the form of eddies and filaments, and also by the northward drift of Agulhas eddies.

The velocity data set comes from a regional ocean model simulation of the Benguela region (Le Vu et al., submitted for publication). The ROMS model (Shchepetkin and McWilliams, 2003, 2005) is a split-explicit free-surface, topography-following model. It solves the incompressible primitive equations using the Boussinesq and hydrostatic approximations. Potential temperature and salinity transport are included by coupling advection/diffusion schemes for these variables. The model was forced with climatological data. The data set area extends from 12°S to 35°S and from 4°E to 19°E (see Fig. 1). The velocity field $\mathbf{u} = (u, v, w)$ consists of 2 years of daily averages of zonal (u), meridional (v), and vertical velocity (w) components, stored in a 3D grid with a horizontal resolution of 1/12 degrees (~8 km) and 32 vertical terrain-following levels using a stretched vertical coordinate where the layer thickness increases from the surface/bottom to the ocean interior. Because the ROMS model considers the hydrostatic approximation, it is important to note that Mahadevan (2006), when comparing the results from non-hydrostatic and hydrostatic versions of the same model of vertical motions at submesoscale fronts, found that while instantaneous vertical velocities structures differed between the versions, the averaged vertical flux is similar in both hydrostatic and non-hydrostatic simulations.
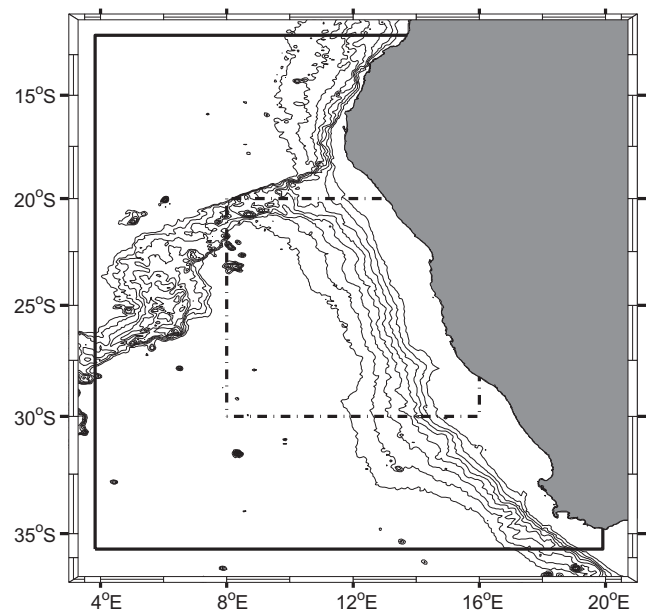

Fig. 1. The Benguela upwelling region. The velocity field domain is limited by the continuous black line. The FSLE calculation area is limited by the dash-dot black line. Bathymetric contour lines are derived from the ETOPO1 global relief model (Amante and Eakins, 2009) starting at a depth of 0 m and ranging up to 4000 m at intervals of 500 m.

2.2. Finite-size Lyapunov exponents

The finite size Lyapunov exponent (Aurell et al., 1997; Artale et al., 1997) is particularly well suited to the study of non-asymptotic dispersion processes such as stretching at finite scales and time intervals. It is defined as:

$$\lambda = \frac{1}{\tau} \log \frac{\delta_f}{\delta_0}, \tag{1}$$

where τ is the time it takes for the separation between two particles, initially δ_0, to reach δ_f. In addition to the dependence on the values of δ_0 and δ_f, the FSLE also depends on the initial position of the particles and on the time of deployment. Locations (i.e., initial positions) leading to high values of this Lyapunov field identify regions of strong separation between particles, i.e., regions that will exhibit strong stretching during evolution, which can be identified with the LCS (Boffetta et al., 2001; d'Ovidio et al., 2004; Joseph and Legras, 2002).

In principle, to compute FSLEs in three dimensions, one only needs to extend the method of d'Ovidio et al. (2004); that is, one needs to compute the time that fluid particles initially separated by $\delta_0 = [(\delta x_0)^2 + (\delta y_0)^2 + (\delta z_0)^2]^{1/2}$ required to reach a final distance of $\delta_f = [(\delta x_f)^2 + (\delta y_f)^2 + (\delta z_f)^2]^{1/2}$. The primary difficulty in this computation is that in the ocean, vertical displacements (even in upwelling regions) are much smaller than the horizontal ones and thus do not contribute significantly to total particle dispersion (Özgökmen et al., 2011). By the time that the scale of horizontal particle dispersion reaches tenths or hundreds of kilometers (typical mesoscale structures are studied using $\delta_f \approx 100$ km (d'Ovidio et al., 2004)), the particle dispersion in the vertical dimension can reach, at most, scales of hundreds of meters, and usually less. This fact means that vertical separation will not contribute significantly to the accumulated distance between particles. In addition, because the length scales of the horizontal and vertical dimensions differ by several orders of magnitude, one faces the impossibility of assigning equal δ_0 to the horizontal and vertical particle pairs. It should be noted, however, that these shortcomings arise from the different scales of length and time that characterize horizontal and vertical dispersion processes in the ocean and thus should not be considered as intrinsic limitations of the method. For non-oceanic flows, a direct generalization of FSLEs is straightforward.

Therefore, in this paper, we implemented a quasi 3D computation of FSLEs. That is, we perform a computation for every (2D) ocean layer, but for the particle trajectories calculation, we use the full 3D velocity field, i.e., at each level (depth), we set $\delta z_0 = 0$, and the final distance is computed without taking the vertical distance between particles. It is important to note that because we allow the particles to evolve in the full 3D velocity field, we take into account vertical quantities such as vertical velocity shear that may influence the horizontal separation between particle pairs.

There are other possible approaches to the issue of different scales in the vertical and horizontal. One such approach is to assign anisotropic initial and final displacements in the FSLE calculation (i.e., including a δz_0 and δz_f that are much smaller than the horizontal initial and final separations). A second approach is to use different weights for the horizontal and vertical separations in the calculations of distance, perhaps in combination with the first approach. We have evaluated both alternatives and found that, with reasonable choices of initial and final distances and distance metrics, the results were equivalent to the quasi-3D computation. The reason for this equivalence is that actual dispersion is primarily horizontal, as noted above.

In more detail, a grid of initial locations $\mathbf{x}_0$ in the longitude/latitude/depth geographical space (ϕ, θ, z), fixing the spatial resolution of the FSLE field, is set up at time t. The horizontal distance among the grid points, δ_0, was set to 1/36 degrees (≈ 3 km), i.e., a resolution three times finer than the velocity field (Hernandez-Carrasco et al., 2011), and the vertical resolution (distance between layers) was set to 20 m to have a good representation of the vertical variations in the FSLE field. Particles are released from each grid point, and their 3D trajectories are calculated. The distances of each particle with respect to the particles that were initially its neighbors at a horizontal distance δ_0 are monitored until one of the horizontal separations reaches a value δ_f. By integrating the 3D particle trajectories backward and forward in time, we obtain two different types of FSLE maps: the attracting LCS (from the backward integration) and the repelling LCS (forward integration) (d'Ovidio et al., 2004; Joseph and Legras, 2002). In this way, we obtain FSLE fields with a horizontal spatial resolution given by δ_0. The final distance δ_f was set to 100 km, which is, as already mentioned, a typical length scale for mesoscale studies. The trajectories were integrated for a maximum of $T = 178$ days (approximately 6 months) using an integration time step of 6 h. When a particle reached the coast or left the velocity field domain, the FSLE value at its initial position and initial time was set to zero. If the interparticle horizontal separation remains smaller than δ_f during all the integration time, then the FSLE for that location is also set to zero.

The equations of motion that describe the evolution of particle trajectories are

$$\frac{d\phi}{dt} = \frac{1}{R_z} \frac{u(\phi, \theta, z, t)}{\cos(\theta)}, \tag{2}$$

$$\frac{d\theta}{dt} = \frac{1}{R_z} v(\phi, \theta, z, t), \tag{3}$$

$$\frac{dz}{dt} = w(\phi, \theta, z, t), \tag{4}$$

where ϕ is longitude, θ is latitude and z is the depth. R_z is the radial coordinate of the moving particle $R_z = R - z$, with $R = 6371$ km the mean Earth radius. For all practical purposes, $R_z \approx R$. Particle trajectories are integrated using a 4th order Runge–Kutta method. For the calculations, one needs the (3D) velocity values at the current location of the particle. Because the 6 grid nodes surrounding the particle do not form a regular cube, direct trilinear interpolation cannot be used. Thus, an isoparametric element formulation is used to map the nodes of the velocity grid surrounding the particle position to a regular cube, and an inverse isoparametric mapping scheme (Yuan et al., 1994) is used to find the coordinates of the interpolation point in the regular cube coordinate system.

2.3. Lagrangian coherent structures

In 2D, LCSs practically coincide with (finite-time) stable and unstable manifolds of relevant hyperbolic structures in the flow (Haller, 2000; Haller and Yuan, 2000; Joseph and Legras, 2002). The structure of these last objects in 3D is generally much more complex than in 2D (Haller, 2001; Pouransari et al., 2010), and locally, they can be either lines or surfaces. As noted earlier, however, vertical movement in the ocean is slow. Thus, at each fluid parcel, the directions of strongest attraction and repulsion should be nearly horizontal. This, combined with the incompressibility property, implies that the most attracting and repelling regions (i.e., the LCSs) should appear as almost vertical surfaces, as the attraction or repulsion should occur normally to the LCS. As a consequence, the LCSs will have a curtain-like" geometry, with deviations from the vertical due either to the orientation of the most attracting or repelling direction deviating from the horizontal or to instances where strong vertical shear produces variations along the vertical in the most repelling or attracting regions in the flow. We expect the LCS sheet-like objects to coincide with the strongest hyperbolic manifolds when these are 2D and to contain the strongest hyperbolic lines.

The curtain-like geometry of the LCS was already commented on in Branicki and Malek-Madani (2010), Branicki and Kirwan (2010) and Branicki et al. (2011). In the latter paper, it was shown that, in a 3D flow, these structures would appear mostly vertical when the ratio of the vertical shear of the horizontal velocity components to the average horizontal velocities is small. This ratio also determines the vertical extension of the structures. In Branicki and Kirwan (2010), this argument was used to construct a 3D model of hyperbolic structures from the computation in a 2D slice. In the present paper, we confirm the curtain-like geometry of the LCSs and show that they are relevant to the organization of the fluid flow in this realistic 3D oceanic setting. This is performed in the next section by comparing actual particle trajectories with the computed LCSs.

In contrast with 2D, where LCSs can be visually identified as the maxima of the FSLE field, in 3D the ridges are hidden within the volume data. Thus, one needs to explicitly compute and extract them using the definition of LCSs as the ridges of the FSLEs. A ridge L is a co-dimension 1 orientable, differentiable manifold (which means that for a 3D domain D, ridges are surfaces), satisfying the following conditions (Lekien et al., 2007):

1. The field λ attains a local extremum at L.
2. The direction perpendicular to the ridge is the direction of the fastest descent of λ at L.

Mathematically, the two previous requirements can be expressed as

$$\mathbf{n}^{\mathrm{T}}\nabla\lambda = 0, \tag{5}$$

$$\mathbf{n}^{\mathrm{T}}\mathbf{H}\mathbf{n} = \min_{\|\mathbf{u}\|=1}\mathbf{u}^{\mathrm{T}}\mathbf{H}\mathbf{u} < 0, \tag{6}$$

where $\nabla\lambda$ is the gradient of the FSLE field λ, $\mathbf{n}$ is the unit normal vector to L and $\mathbf{H}$ is the Hessian matrix of λ.

The method used to extract the ridges from the scalar field $\lambda(\mathbf{x}_0,t)$ is from Schultz et al. (2010). It utilizes an earlier (Eberly et al., 1994) definition of ridge in the context of image analysis as a generalized local maxima of scalar fields. For a scalar field $f : \mathbb{R}^n \rightarrow \mathbb{R}$ with gradient $\mathbf{g} = \nabla f$ and Hessian $\mathbf{H}$, a d-dimensional height ridge is given by the conditions

$$\forall_{d<i\leqslant n} \quad \mathbf{g}^{\mathrm{T}}\mathbf{e}_i = 0 \text{ and } \alpha_i < 0, \tag{7}$$

where α_i, $i \in \{1,2,\ldots,n\}$, are the eigenvalues of $\mathbf{H}$, ordered such that $\alpha_1 \geqslant \cdots \geqslant \alpha_n$, and $\mathbf{e}_i$ is the eigenvector of $\mathbf{H}$ associated with α_i. For $n = 3$, (7) becomes

$$\mathbf{g}^{\mathrm{T}}\mathbf{e}_3 = 0 \text{ and } \alpha_3 < 0. \tag{8}$$

This ridge definition is equivalent to the one given by (5) because the unit normal $\mathbf{n}$ is the eigenvector (when normalized) associated with the minimum eigenvalue of $\mathbf{H}$. In other words, in $\mathbb{R}^3$ the $\mathbf{e}_1$, $\mathbf{e}_2$ eigenvectors point locally along the ridge, and the $\mathbf{e}_3$ eigenvector is orthogonal to it.

The ridges extracted from the backward FSLE map approximate the attracting LCS, and the ridges extracted from the forward FSLE map approximate the repelling LCS. The attracting LCSs are the more interesting from a physical point of view (d'Ovidio et al., 2004, 2009), as particles (or any passive scalar driven by the flow) typically approach them and spread along them, giving rise to filament formation. In the extraction process, it is necessary to specify a threshold s for the ridge strength $|\alpha_3|$, so that the ridge points whose value of α_3 is lower (in absolute value) than s are discarded from the extraction process. Because the ridges are constructed by triangulations of the set of extracted ridge points, the s threshold greatly determines the size and shape of the extracted ridge by filtering out regions of the ridge that have low strength. The reader is

referred to Schultz et al. (2010) for details about the ridge extraction method. The height ridge definition has been used to extract LCSs from FTLE fields in several works (see, among others, Sadlo and Peikert (2007)).

3. Results

3.1. Three-dimensional FSLE field

The 3D FSLE field was calculated for a 30-day period beginning on September 17 of year 8 of the ROMS simulation period, with snapshots taken every 2 days. The fields were calculated for an area of the Benguela ocean region between latitudes 20°S and 30°S and longitudes 8°E and 16°E (see Fig. 1). The area is bounded in the NW by the Walvis Ridge, and the continental slope approximately bisects the region from NW to SE. The western half of the domain has abyssal depths of approximately 4000 m. The calculation domain extended vertically from 20 up to 580 m in depth. Both backward and forward calculations were made to extract the attracting and repelling LCSs.

Fig. 2 displays the vertical profile of the average FSLE for the 30-day period. There are small differences between the backward and the forward values due to the different intervals of time involved in their calculation, but both profiles have a similar shape and show a general decrease with depth. There is a notable peak in the profiles at a depth of approximately 100 m that indicates increased mesoscale variability (and transport, as shown in Section 3.2 at that depth).

A snapshot of the attracting LCSs for day 1 of the calculation period is shown in Fig. 3. As expected, the structures appear as thin vertical curtains, most of them extending throughout the depth of the calculation domain. The area is populated with LCSs, denoting the intense mesoscale activity in the Benguela region. As already mentioned, in three dimensions, the ridges are not easily observed because they are hidden in the volume data. However, the horizontal slices of the field in Fig. 3 indicate that the attracting LCSs fall along the maximum backward FSLE field lines of the 2D slices. The repelling LCSs (not shown) also fall along the maximum forward FSLE field lines of the 2D slices.

Because the λ value of a point on the ridge and the ridges strength α_3 are only related through the expressions (7) and (8),
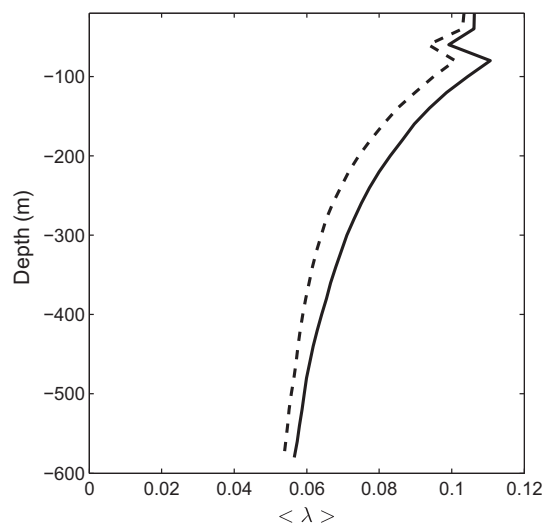

Fig. 2. Vertical profile of 30-day average backward and forward FSLEs. The 30-day average field was spatially averaged at each layer over the FSLE calculation area to produce the vertical profiles. The backward FSLE average is shown in continuous and the forward FSLE is shown in dashed.
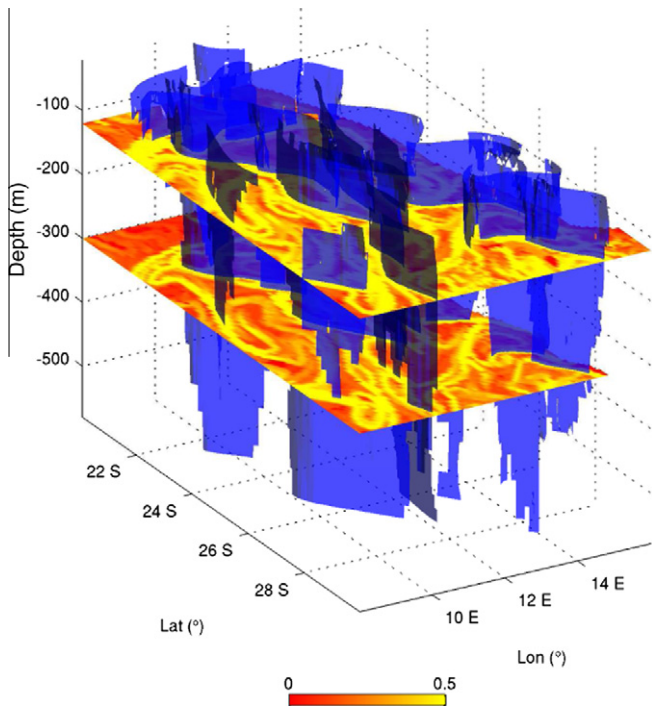
Fig. 3. Attracting LCSs (blue) for day 1 of the calculation period, together with horizontal slices of the backward FSLE field at 120 m and 300 m depths. The color bar refers to the color map of horizontal slices. The units of the color bar are day^{-1}. (For interpretation of the references to colour in this figure legend, the reader is referred to the web version of this article.)

Fig. 4. Trajectory (advancing from NE to SW) of the eddy center inside the calculation domain. Circles indicate the location of the eddys center during the 30-day FSLE calculation period, and squares indicate previous and later positions. Bathymetric lines are the same as in Fig. 1.

the relationship between the two quantities is not direct. This creates a difficulty in choosing the appropriate strength threshold for the extraction process. A value of s that is too small will result in very small LCSs that appear to have little influence on dynamics, whereas a greater value will result in only a partial rendering of the LCS, limiting the possibility of observing their real impact on the flow. Computations with several values of s lead us to the optimum choice $s = 20 \, \text{day}^{-1} \, \text{m}^{-2}$, meaning that grid nodes with $\alpha_3 < -20 \, \text{day}^{-1} \, \text{m}^{-2}$ were filtered out from the LCS triangulation.

We have observed in this section an example of how the ridges of the 3D FSLE field, the LCSs, are distributed in the Benguela ocean region. Their ubiquity signifies their impact on transport and mixing properties. In the next section, we concentrate on the properties of a single 3D mesoscale eddy.

3.2. Study of the dynamics of a relevant mesoscale eddy

Let us study a prominent cyclonic eddy observed in the data set. The trajectory of the center of the eddy was tracked and is shown in Fig. 4. The eddy was apparently pinched off at the upwelling front. At day 1 of the FSLE calculation period, its center was located at latitude 24.8°S and longitude 10.6°E, leaving the continental slope and having a diameter of approximately 100 km. One may ask, what is its vertical size? Is it really a barrier, at any depth, to particle transport?

To properly answer these questions, the eddy, in particular its frontiers, should be located. From the Eulerian point of view, it is commonly accepted that eddies are delimited by closed contours of vorticity and that the existence of strong vorticity gradients prevents transport into and out of the eddy. Such transport may occur when the eddy is destroyed or undergoes strong interactions with other eddies (Provenzale, 1999). From a Lagrangian view point, however, an eddy can be defined as a region delimited by the intersections and tangencies of LCSs, whether in 2D or 3D space. The
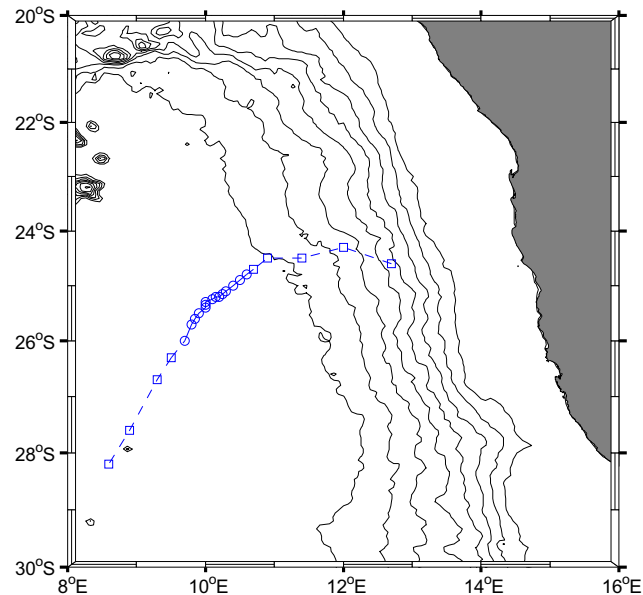
eddy itself is an elliptic structure (Haller and Yuan, 2000; Branicki and Kirwan, 2010; Branicki et al., 2011). In this Lagrangian view of an eddy, the inhibition of transport into and out of the eddy is now related to the existence of these transport barriers delimiting the eddy region, which are known to be quasi-impermeable.

Using the first approach, i.e., the Eulerian view, the vertical distribution of the Q-criteria (Hunt et al., 1988; Jeong and Hussain, 1995) was used to determine the vertical extension of the mesoscale eddy. The Q criterion is a 3D version of the Okubo–Weiss criterion (Okubo, 1970; Weiss, 1991) and measures the relative strengths of vorticity and straining. In this context, eddies are defined as regions with positive Q, with Q the second invariant of the velocity gradient tensor

$$Q = \frac{1}{2}(\|\mathbf{\Omega}\|^2 - \|\mathbf{S}\|^2), \tag{9}$$

where $\|\mathbf{\Omega}\|^2 = tr(\mathbf{\Omega}\mathbf{\Omega}^T)$, $\|\mathbf{S}\|^2 = tr(\mathbf{S}\mathbf{S}^T)$ and $\mathbf{\Omega}$, $\mathbf{S}$ are the antisymmetric and symmetric components of $\nabla \mathbf{u}$. Using $Q = 0$ as the Eulerian eddy boundary, it can be observed from Fig. 5 that the eddy extends vertically down to at least 600 m.

Let us move to the Lagrangian description of eddies, which is more in the spirit of our study and will allow us to study particle transport: eddies can be defined as the region bounded by intersecting or tangential repelling and attracting LCSs (Branicki and Kirwan, 2010; Branicki et al., 2011). Using this criterion and first looking at the surface located at a depth of 200 m, we observe in Fig. 6 that the Eulerian eddy certainly appears to be located inside the area defined by several intersections and tangencies of LCSs. This eddy has an approximate diameter of 100 km. In the south-north direction, there are two intersections that appear to be hyperbolic points (H1 and H2 in Fig. 6). In the west-east direction, the eddy is closed by a tangency at the western boundary and an intersection of lines at the eastern boundary. The eddy core is devoid of high FSLE lines, indicating that weak stirring occurs inside (d'Ovidio et al., 2004). As additional Eulerian properties, we note that near or at the intersections H1 and H2, the Q-criterion indicates straining motions. In the case of H2, Fig. 5 (right panel) indicates high shear up to a depth of 200 m. The fact that the hyperbolic regions H1 and
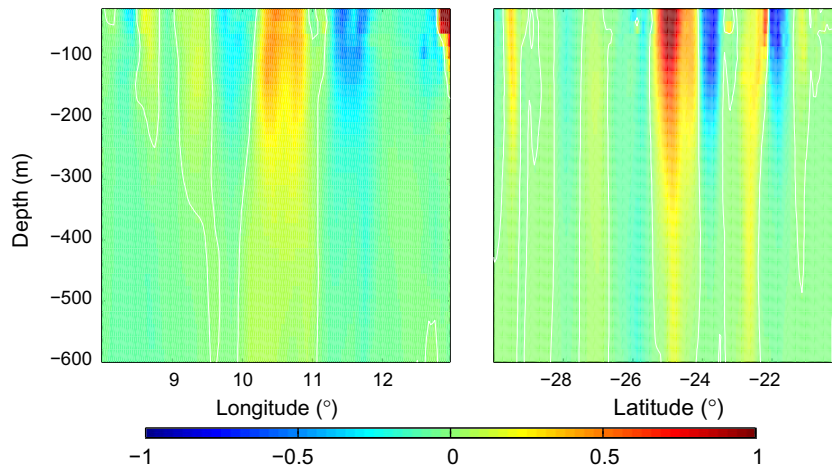
Fig. 5. Color map of Q-criterion. White contours have Q = 0. Day 1 of the 30-day FSLE calculation period. Left panel: latitude 24.5°S; Right panel: longitude 10.5°E. Color bar values are $Q \times 10^{10}$ s^{-2}. (For interpretation to colours in this figure, the reader is referred to the web version of this article.)
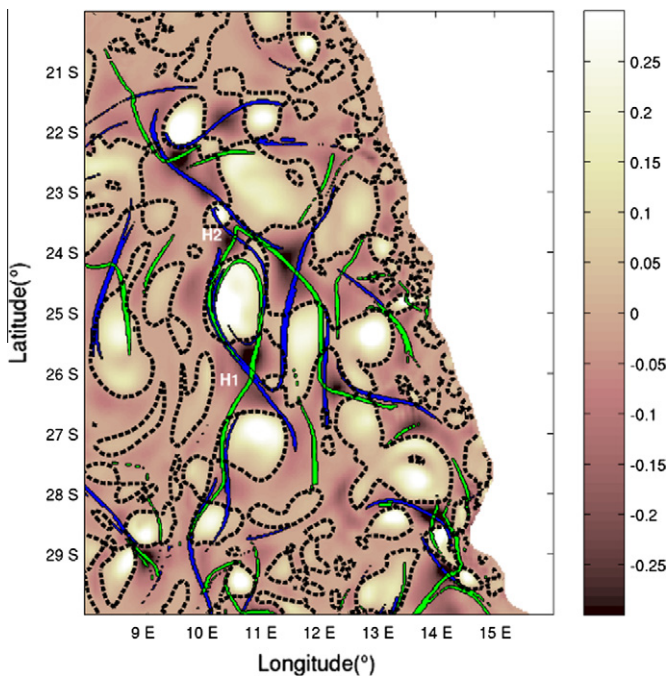

Fig. 6. Q-criterion map at a depth of 200 m together with patches of backward (blue) and forward (green) FSLE values. Black dashed lines have Q = 0. FSLE patches contain the highest 60% of FSLE values. Color bar values are $Q \times 10^{10}$ s^{-2}. The eddy we study is the clear region in between points H1 and H2. (For interpretation of the references to colour in this figure legend, the reader is referred to the web version of this article.)

H2 lie in strain-dominated regions of the flow (Q < 0) highlights the connection between hyperbolic particle behavior and instantaneous hyperbolic regions of the flow. The ridges of the FSLE field, however, do not remain in the negative Q regions but cross into rotation-dominated regions with Q > 0. This finding indicates that there are some differences between the Eulerian view (Q) and the Lagrangian view (FSLE). It is the latter that can be understood in terms of particle behavior as limiting regions of initial conditions (particles) that stay away from hyperbolic regions for a long enough time (Haller and Yuan, 2000).

In 3D, the eddy is also surrounded by a set of attracting and repelling LCSs (Fig. 7), calculated as described in Section 2.3. The lines identified in Fig. 6 are now considered to belong to these vertical surfaces.

Note that the vertical extents of these surfaces are determined in part by the strength parameter used in the LCS extraction process, and thus, their true vertical extension is not clear from the results presented here. To the south, the closure of the Lagrangian eddy boundary extends down to the maximum depth of the calculation domain, but moving northward, it is observed that the LCSs decrease in depth. Most likely, this does not mean that the eddy is shallower in the north but rather that the LCSs are losing strength (lower $|\alpha_3|$) and that portions of the LCs are filtered out by the extraction process. In any case, it is observed that as in 2D calculations, the LCSs delimiting the eddy do not perfectly coincide with its Eulerian boundary (Joseph and Legras, 2002), and we expect the Lagrangian view to be more relevant for addressing transport questions.

In the next paragraphs, we analyze the fluid transport across the eddy boundary. Some previous results for Lagrangian eddies were obtained by Branicki and Kirwan (2010) and Branicki et al. (2011). Applying the methodology of lobe dynamics and the turnstile mechanism to eddies pinched off from the Loop Current, Branicki and Kirwan (2010) observed a net fluid entrainment near the base of the eddy and net detrainment near the surface, with fluid transport into and out of the eddy being essentially confined to the boundary region.

We consider six sets of 1000 particles each that were released on day 1 of the FSLE calculation period and their trajectories, integrated by a 4th-order Runge–Kutta method with an integration time step of 6 h. The sets of particles were released at depths of 50, 100, 200, 300, 400 and 500 m. In Fig. 8, we plot the particle sets together with the Lagrangian boundaries of the mesoscale eddy viewed in 3D. A top view is shown in Fig. 9. As expected, the vertical displacements are small.

At day 3 (top left panel of Figs. 8 and 9), it can be observed that there is a differential rotation (generally cyclonic, i.e., clockwise) between the sets of particles at different depths. The shallower sets rotate more quickly than the deeper ones. This differential rotation of the fluid particles could be viewed from a Lagrangian perspective as a result of the attracting and repelling strengths of the LCSs that limit the eddy varying with depth. Note that the sets of particles are released at the same time and at the same horizontal position, and thus, differences in their behavior are due to the variations of the LCS properties with depth.

At day 13, the vortex starts to expel material through filamentation (Figs. 8 and 9, top right panels). A fraction of the particles approach the southern boundaries of the eddy from the northeast. Those to the west of the repelling LCS (green) turn west and
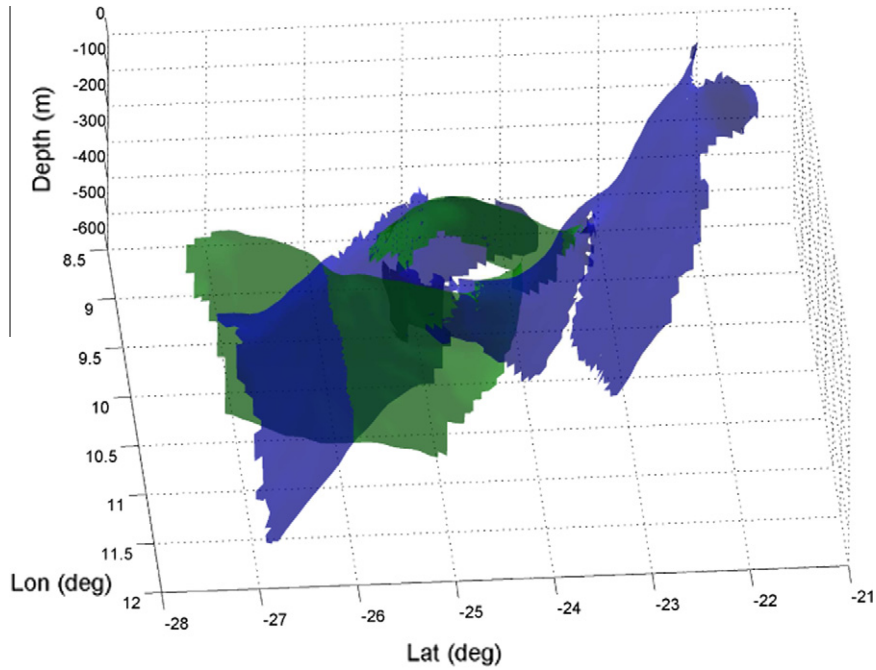
Fig. 7. Three-dimensional LCSs around the mesoscale eddy at day 1 of the 30-day FSLE calculation period. Green: repelling LCSs; Blue: attracting LCSs. (For interpretation of the references to colour in this figure legend, the reader is referred to the web version of this article.)
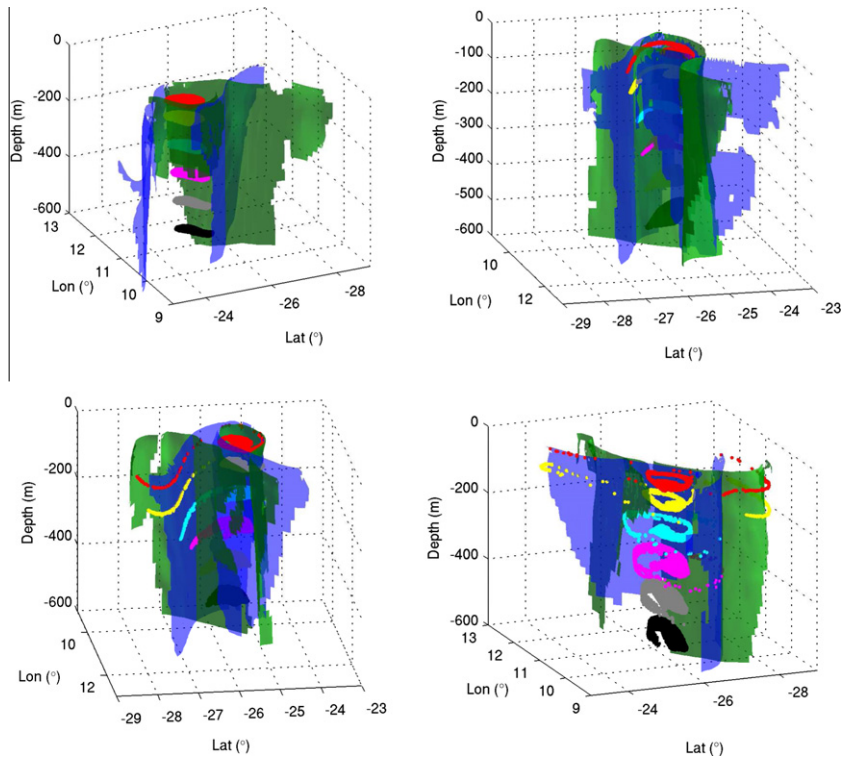

Fig. 8. Three-dimensional view of the evolution of elliptic patches released at different depths inside of the eddy on day 1 of the 30-day FSLE calculation period. Top left: day 3; top right: day 13; bottom left: day 19: bottom right: day 29. Red: 40 m; yellow: 100 m; cyan: 200 m; magenta: 300 m; grey: 400 m; black: 500 m. Attracting LCSs are shaded in blue, whereas repelling LCSs are shaded in green. (For interpretation of the references to colour in this figure legend, the reader is referred to the web version of this article.)

recirculate inside the eddy along the southern attracting LCS (blue). Particles to the east of the repelling LCS turn east and leave the eddy, forming a filament aligned with an attracting (blue) LCS. Later, trajectories to the south of the eddy are influenced by additional structures associated with a different southern eddy. At day

29 (bottom right panels), the same process can be observed to have occurred in the northern boundary, with a filament of particles leaving the eddy along the northern attracting (blue) LCS. This filamentation appears to begin earlier in shallower water than at greater depths because the length of the expelled filament
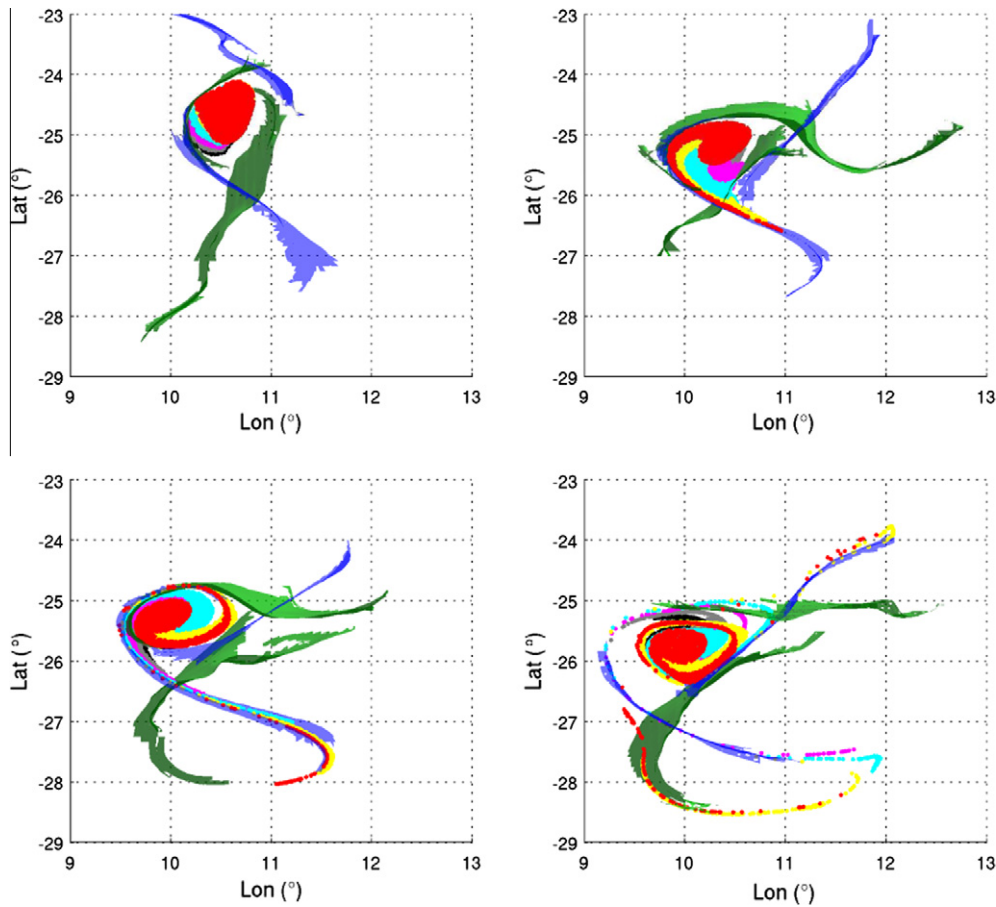
Fig. 9. Top view of the evolution of particle patches and LCSs shown in Fig. 8. Top left: day 3; top right: day 13; bottom left: day 19; bottom right: day 29. Colors as in Fig. 8.

diminishes with depth. However, all of the expelled filaments follow the same attracting LCS. Fig. 10 illustrates the stages previous to filamentation, in which the structure of the LCSs, their tangencies and intersections, and the paths of the particle patches are more clearly visible. Note that the LCSs do not form fully closed structures and that the particles can escape the eddy through the resulting openings. The images suggest lobe-dynamics processes, but much higher precision in the LCS extraction would be needed to optimally observe such details.

This filamentation event appears to be the only mechanism responsible for the transportation of material outside of the eddy, as the rest of the particles remained inside the eddy boundaries. To obtain a rough estimate of the amount of matter expelled in the filamentation process, we tracked the percentage of particles leaving a 200 km diameter circle centered on the eddy center. In Fig. 11, the change in this percentage over time is illustrated for the particle sets released at different depths. The onset of filamentation is clearly visible around days 9–12 as a sudden increase in the percentage of particles leaving the eddy. The percentage is highest for the particles located at a 100 m depth and decreases as the depth increases. At depths of 400 and 500 m, there are no particles leaving the circle. There is a clear lag in the onset of filamentation between the different depths: the onset is simultaneous for the 40 m and 100 m depths but occurs later for greater depths.

4. Discussion

The spatial average of FSLEs defines a measure of stirring and thus of horizontal mixing between the scales used for its computation. The larger the average, the larger the mixing activity (d'Ovidio

et al., 2004). The general trend in the vertical profiles of the average FSLE (Fig. 3) shows a reduction in mesoscale mixing with depth. There is, however, a rather interesting peak in this average profile occurring at 100 m, i.e., close to the thermocline. This peak could be related to submesoscale processes that occur alongside the mesoscale ones. The submesoscale is associated with filamentation (the thickness of filaments is on the order of 10 km or less), and we have observed that filamentation and the associated transport intensity (Fig. 11) are higher at a 100 m depth. It is not clear at the moment what the precise mechanism responsible for this increased activity at depths of approximately 100 m might be (perhaps associated with instabilities in the mixed layer), but we note that the intensity of shearing motions (see the Q plots in Fig. 5) is higher within 200 m of the ocean surface. Less intense filamentation could be caused by the reduction of shear at depths greater than those values.

From an Eulerian perspective, it is thought that vortex filamentation occurs when the potential vorticity (PV) gradient aligns itself with the compressional axis of the velocity field in strain coordinates (Louazel and Hua, 2004; Lapeyre et al., 1999). This alignment is accompanied by exponential growth of the PV gradient magnitude. The fact that filamentation occurs along the attracting LCSs appears to indicate that this exponential growth of the PV gradient magnitude occurs across the attracting LCSs.

In the specific spatiotemporal area studied here and, in particular, for the eddy on which we focused our analysis, we have confirmed that the structure of the LCSs is curtain-like" such that the strongest attracting and repelling structures are quasivertical surfaces. Their vertical extension would depend on physical transport properties but is also altered by the particular threshold
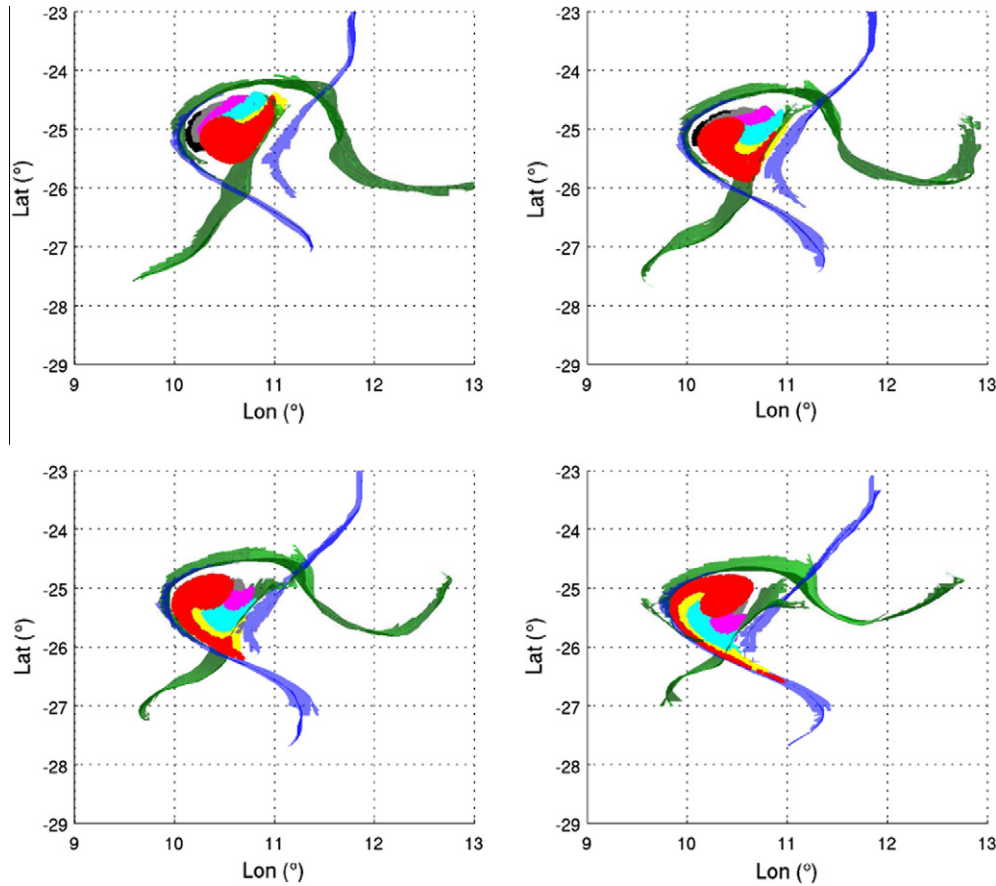
Fig. 10. Top view of the initial stages of evolution of the particle patches and LCSs of Figs. 8 and 9. Top left: day 7; top right: day 9; bottom left: day 11; bottom right: day 13. Colors as in Fig. 8.
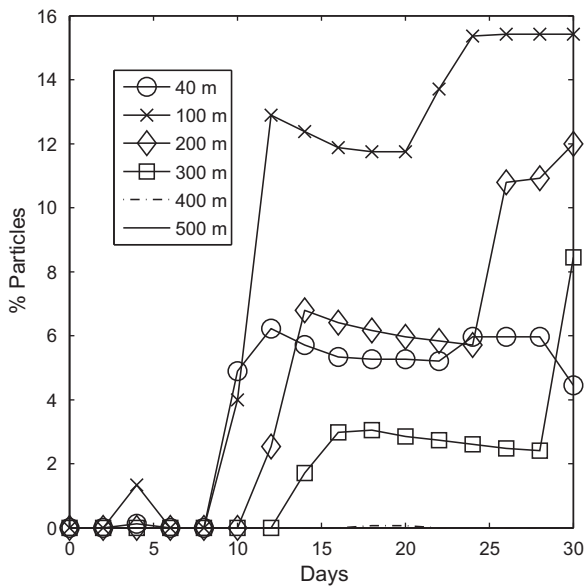

Fig. 11. Percentage of particles outside a 200 km diameter circle centered at the eddy center as a function of time.

parameter used to extract the LCSs. These observations imply that transport and stirring occur primarily in the horizontal dimension, which is a reasonable result considering the disparity between horizontal and vertical velocities in the ocean and the oceans vertical stratification. However, we should mention that our results are not fully generalizable to all ocean situations and that any ocean area or oceanic event should be studied independently to reveal the shape of its associated 3D LCSs.

Some comments follow about the nature of vertical transport structures. FSLEs are suited to the identification of hyperbolic structures (structures that exhibit high rates of transversal stretching or compression in their vicinity). Thus, the question, then,is whether one can expect that structures responsible for vertical transport will also exhibit substantial (vertical) stretching. This is not so clear in the ocean for the reasons already indicated. If one considers the case (relevant to our work) of purely isopycnal flow, then strong vertical stretching would be associated with a rapid divergence of isopycnic surfaces. In the case of coastal upwelling, for instance, the lifted isopycnic surfaces move vertically in a coherent fashion, so one should not expect strong vertical divergence of particles flowing along neighboring isopycnic surfaces. This is merely an example of the fact that it is possible that coherent vertical motions do not imply the presence of hyperbolic coherent structures such as those the FSLE may indicate.

Another possible limitation worth noting is the velocity field resolution and its relation to the intensity of the vertical velocity. It is accepted that in fronts or in the periphery of eddies, vertical velocities are significantly greater than, for instance, in the eddy interior. These zones of enhanced vertical transport correspond to submesoscale features that were not adequately captured in the velocity field used in this work due to its coarse resolution because submesoscale studies usually have resolutions <10 km (the literature on this subject is quite extensive, so we refer the reader to Klein and Lapeyre (2009) and Lévy (2008)).

In any case, a most important point for the LCSs we have computed is that in 3D, as in 2D, LCSs act as pathways and barriers to transport, thus providing a skeleton organizing the transport processes.

5. Conclusions

Three-dimensional Lagrangian coherent structures were used to study the stirring processes leading to dispersion and mixing at the mesoscale in the Benguela ocean region. We have computed 3D finite size Lyapunov exponent fields, and LCSs were identified with the ridges of these fields. LCSs appear as quasivertical surfaces such that horizontal cuts of the FSLE fields provide a highly accurate vision of the 3D FSLE distribution. These quasivertical surfaces appear to be coincident with the maximal lines of the FSLE field (see Fig. 3) such that surface FSLE maps could be indicative of the position of 3D LCSs, as long as the vertical shear of the velocity does not result in a significant deviation of the LCS with respect to the vertical. Average FSLE values generally decrease with depth, but we find a local maximum and thus enhanced stretching and dispersion, at a depth of approximately 100 m.

We have also analyzed a prominent cyclonic eddy that was pinched off from the upwelling front and studied its filamentation dynamics in 3D. The Lagrangian boundaries of the eddy were upcomposed of the intersections and tangencies of attracting and repelling LCSs apparently emanating from two hyperbolic locations north and south of the eddy. The LCSs were observed to provide pathways and barriers organizing the processes and geometry of transport into and out of the eddy. This pattern extends down, up to the maximum depth for which we calculated the FSLE fields ($\sim$600 m), but the exact shape of the boundary is difficult to determine due to the decrease in ridge strength with depth. This issue caused some parts of the LCSs not to be extracted. The inclusion of a variable strength parameter in the extraction process is an important step to be included in the future.

Filamentation dynamics, and thus transportation out of the eddy, showed time lags with increasing depth. This observation arises from the vertical variation of the flow field. However, filamentation occurred across all depths, indicating that in reality, vertical sheets of material are expelled from these eddies.

Many additional studies are needed to further clarify the details of the geometry of the LCSs, their relationships with finite-time hyperbolic manifolds and 3D lobe dynamics, and especially their interplay with mesoscale and submesoscale transport and mixing processes.

Acknowledgements

References

Amante, C., Eakins, B.W., 2009. ETOPO1 1 Arc-Minute Global Relief Model: Procedures, Data Sources and Analysis. NOAA Technical Memorandum NESDIS NGDC-24.
Artale, V., Boffetta, G., Celani, A., Cencini, M., Vulpiani, A., 1997. Dispersion of passive tracers in closed basins: beyond the diffusion coefficient. Phys. Fluids 9, 3162–3171.

Aurell, E., Boffetta, G., Crisanti, A., Paladin, G., Vulpiani, A., 1997. Predictability in the large: an extension of the Lyapunov exponent. J. Phys. A 30, 1–26.
Beron-Vera, F., Olascoaga, M., Goni, G., 2008. Oceanic mesoscale eddies as revealed by Lagrangian coherent structures. Geophys. Res. Lett. 35, L12603.
Boffetta, G., Lacorata, G., Redaelli, G., Vulpiani, A., 2001. Detecting barriers to transport: a review of different techniques. Physica D 159, 58–70.
Branicki, M., Kirwan, A., 2010. Stirring: the Eckart paradigm revisited. Int. J. Eng. Sci. 48, 1027–1042.
Branicki, M., Malek-Madani, R., 2010. Lagrangian structure of flows in the Chesapeake Bay: challenges and perspectives on the analysis of estuarine flows. Nonlinear Proc. Geophys. 17, 149–168.
Branicki, M., Mancho, A.M., Wiggins, S., 2011. A Lagrangian description of transport associated with a front-eddy interaction: application to data from the North-Western Mediterranean sea. Phys. D: Nonlinear Phenom. 240, 282–304.
Branicki, M., Wiggins, S., 2009. Finite-time Lagrangian transport analysis: stable and unstable manifolds of hyperbolic trajectories and finite-time Lyapunov exponents. Nonlinear Proc. Geophys. 17, 1–36.
Byrne, D.A., Gordon, A.L., Haxby, W.F., 1995. Agulhas eddies: a synoptic view using Geosat ERM data. J. Phys. Oceanogr. 25, 902–917.
Doglioli, A., Blanke, B., Speich, S., Lapeyre, G., 2007. Tracking coherent structures in a regional ocean model with wavelet analysis: application to cape basin eddies. J. Geophys. Res. C: Oceans 112, C05043.
d'Ovidio, F., Fernández, V., Hernández-García, E., López, C., 2004. Mixing structures in the Mediterranean sea from finite-size Lyapunov exponents. Geophys. Res. Lett. 31, L17203.
d'Ovidio, F., Isern, J., López, C., Hernández-García, E., García-Ladona, E., 2009. Comparison between Eulerian diagnostics and finite-size Lyapunov exponents computed from Altimetry in the Algerian basin. Deep-Sea Res. I 56, 15–31.
Eberly, D., Gardner, R., Morse, B., Pizer, S., Scharlach, C., 1994. Ridges for image analysis. J. Math. Imaging Vis. 4, 353–373.
Elhmaïdi, D., Provenzale, A., Babiano, A., 1993. Elementary topology of 2D turbulence from a Lagrangian viewpoint and single-particle dispersion. J. Fluid Mech. 257, 533–558.
Haller, G., 2000. Finding finite-time invariant manifolds in 2D velocity fields. Chaos 10 (1), 99–108.
Haller, G., 2001. Distinguished material surfaces and coherent structure in 3D fluid flows. Physica D 149, 248–277.
Haller, G., 2002. Lagrangian coherent structures from approximate velocity data. Phys. Fluids A14, 1851–1861.
Haller, G., 2011. A variational theory of hyperbolic lagrangian coherent structures. Physica D 240, 574–598.
Haller, G., Yuan, G., 2000. Lagrangian coherent structures and mixing in 2D turbulence. Physica D 147, 352–370.
Haza, A., Özgökmen, T., Griffa, A., Molcard, A., Poulain, P.M., Peggion, G., 2010. Transport properties in small-scale coastal flows: relative dispersion from VHF radar measurements in the Gulf of La Spezia. Ocean Dynam. 60, 861–882.
Haza, A.C., Poje, A.C., Özgökmen, T.M., Martin, P., 2008. Relative dispersion from a high-resolution coastal model of the Adriatic Sea. Ocean Model. 22, 48–65.
Hernandez-Carrasco, I., López, C., Hernández-García, E., Turiel, A., 2011. How reliable are finite-size Lyapunov exponents for the assessment of ocean dynamics? Ocean Model. 36, 208–218.
Hunt, J.C.R., Wray, A.A., Moin, P., 1988. Eddies, Streams and Convergence Zones in Turbulent Flows. Technical Report CTR-S88. Center for Turbulence Research, Standford University, pp. 193–208.
Jeong, J., Hussain, F., 1995. On the identification of a vortex. J. Fluid Mech. 285, 69–94.
Joseph, B., Legras, B., 2002. Relation between kinematic boundaries, stirring, and barriers for the Antarctic polar vortex. J. Atmos. Sci. 59, 1198–1212.
Klein, P., Lapeyre, G., 2009. The oceanic vertical pump induced by mesoscale and submesoscale turbulence. Ann. Rev. Mar. Sci. 1, 351–375.
Lacasce, J., 2008. Statistics from Lagrangian observations. Prog. Oceanogr. 77, 1–29.
Lapeyre, G., Klein, P., Hua, B., 1999. Does the tracer gradient vector align with strain eigenvectors in 2D turbulence? Phys. Fluids 11, 3729–3737.
Le Vu, B., Gutknecht, E., Machu, E., Dadou, I., Veitch, J., Sudre, J., Paulmier, A., Garçon, V., submitted for publication. Processes maintaining the OMZ of the Benguela upwelling system using an eddy resolving model. JMR.
Lehahn, Y., d'Ovidio, F., Lévy, M., Amitai, Y., Heifetz, E., 2011. Long range transport of a quasi isolated chlorophyll patch by an Agulhas ring. Geophys. Res. Lett. 38, L16610.
Lekien, F., Shadden, S.C., Marsden, J.E., 2007. Lagrangian coherent structures in n-dimensional systems. J. Math. Phys. 48, 065404.
Louazel, S., Hua, B.L., 2004. Vortex erosion in a shallow-water model. Phys. Fluids 16, 3079–3085.
Lévy, M., 2008. The modulation of biological production by oceanic mesoscale turbulence. In: Weiss, J., Provenzale, A. (Eds.), Transport and Mixing in Geophysical Flows, Lecture Notes in Physics, vol. 744. Springer, Berlin/Heidelberg, pp. 219–261.
Mahadevan, A., 2006. Modeling vertical motion at ocean fronts: are nonhydrostatic effects relevant at submesoscales? Ocean Model. 14, 222–240.
Mancho, A.M., Small, D., Wiggins, S., 2006. A tutorial on dynamical systems concepts applied to Lagrangian transport in ocean flows defined as finite time data sets: theoretical and computational issues. Phys. Rep. 437, 55–124.
Mariano, A.J., Griffa, A., Özgökmen, T., Zambianchi, E., 2002. Lagrangian analysis and predictability of coastal and ocean dynamics 2000. J. Atmos. Oceanic Technol. 19, 1114–1126.

McGillicuddy, D.J., Robinson, A.R., Siegel, D.A., Jannasch, H.W., Johnson, R., Dickey, T.D., McNeil, J., Michaels, A.F., Knap, A.H., 1998. Influence of mesoscale eddies on new production in the Sargasso sea. Nature 394, 263–266.

Molcard, A., Poje, A., Özgökmen, T., 2006. Directed drifter launch strategies for Lagrangian data assimilation using hyperbolic trajectories. Ocean Model. 12, 268–289.

Okubo, A., 1970. Horizontal dispersion of floatable particles in the vicinity of velocity singularities such as convergences. Deep-Sea Res. I 17, 445–454.

Oschlies, A., Garçon, V., 1998. Eddy-induced enhancement of primary productivity in a model of the North Atlantic ocean. Nature 394, 266–269.

Özgökmen, T.M., Poje, A.C., Fischer, P.F., Haza, A.C., 2011. Large eddy simulations of mixed layer instabilities and sampling strategies. Ocean Model. 39, 311–331.

Pauly, D., Christensen, V., 1995. Primary production required to sustain global fisheries. Nature 374, 255–257.

Poje, A.C., Haza, A.C., Özgökmen, T.M., Magaldi, M.G., Garraffo, Z.D., 2010. Resolution dependent relative dispersion statistics in a hierarchy of ocean models. Ocean Model. 31, 36–50.

Pouransari, Z., Speetjens, M., Clercx, H., 2010. Formation of coherent structures by fluid inertia in 3D laminar flows. J. Fluid Mech. 654, 5–34.

Provenzale, A., 1999. Transport by coherent barotropic vortices. Ann. Rev. Fluid Mech. 31, 55–93.

Rossi, V., López, C., Sudre, J., Hernández-García, E., Garçon, V., 2008. Comparative study of mixing and biological activity of the Benguela and Canary upwelling systems. Geophys. Res. Lett. 35, L11602.

Rubio, A., Blanke, B., Speich, S., Grima, N., Roy, C., 2009. Mesoscale eddy activity in the southern Benguela upwelling system from satellite altimetry and model data. Prog. Oceanogr. 83, 288–295.

Sadlo, F., Peikert, R., 2007. Efficient visualization of Lagrangian coherent structures by filtered AMR ridge extraction. IEEE Trans. Vis. Comput. Graph. 13, 1456–1463.

Schultz, T., Theisel, H., Seidel, H.P., 2010. Crease surfaces: from theory to extraction and application to diffusion tensor MRI. IEEE Trans. Vis. Comput. Graph. 16, 109–119.

Shadden, S.C., Lekien, F., Marsden, J.E., 2005. Definition and properties of Lagrangian coherent structures from finite-time Lyapunov exponents in 2D aperiodic fows. Physica D 212, 271–304.

Shchepetkin, A.F., McWilliams, J.C., 2003. A method for computing horizontal pressure-gradient force in an oceanic model with a nonaligned vertical coordinate. J. Geophys. Res. 108, 3090.

Shchepetkin, A.F., McWilliams, J.C., 2005. The regional ocean modeling system: a split-explicit, free-surface, topography following coordinates ocean model. Ocean Model. 9, 347–404.

Tallapragada, P., Ross, S.D., Schmale III, D.G., 2011. Lagrangian coherent structures are associated with fluctuations in airborne microbial populations. Chaos 21, 033122.

Tang, W., Chan, P.W., Haller, G., 2011. Lagrangian coherent structure analysis of terminal winds detected by lidar. Part I: Turbulence structures. J. Appl. Meteorol. Climat. 50, 325–338.

Thomas, L., Tandon, A., Mahadevan, A., 2008. Submesoscale ocean processes and dynamics. In: Hecht, M., Hasume, H. (Eds.), Ocean Modeling in an Eddying Regime, Geophysical Monograph, vol. 177. American Geophysical Union, Washington DC, pp. 17–38.

du Toit, P., Marsden, J., 2010. Horseshoes in hurricanes. J. Fixed Point Theory Appl. 7, 351–384.

Waugh, D.W., Abraham, E.R., Bowen, M.M., 2006. Spatial variations of stirring in the surface ocean: a case of study of the Tasman sea. J. Phys. Oceanogr. 36, 526–542.

Weiss, J., 1991. The dynamics of enstrophy transfer in 2D hydrodynamics. Physica D 48, 273–294.

Yuan, K.Y., Huang, Y.S., Yang, H.T., Pian, T.H.H., 1994. The inverse mapping and distortion measures for 8-node hexahedral isoparametric elements. Comput. Mech. 14, 189–199.